Microstructure-Linked Mechanical Properties of P91-Incoloy 800HT Dissimilar Metal Welds

The impact of multiple weld passes on microstructure in the heat-affected zone and weld fusion zone was investigated

BY V. BHANU, A. GUPTA, AND C. PANDEY

Abstract

Dissimilar metal welds (DMWs) between P91 steel and Incoloy 800HT® using shielded metal arc welding (SMAW) with ENiCrCoMo-1 filler electrode were characterized in detail. The impact of multiple weld passes on microstructure in the heat-affected zone (HAZ) and weld fusion zone (WFZ) was thoroughly investigated. Postweld heat treatment (PWHT) impacts on mechanical characteristics and microstructure were also observed. The DMW was observed with heavy C, Cr, and Mo microsegregation in the WFZ, which deteriorated mechanical strength. The microstructural changes directly affected the mechanical behavior of the DMW. The ultimate tensile strength of the weld fusion zone was low at 576 MPa compared to the base metals' strength. The tensile specimens failed in the IN 800HT base metal and WFZ. The WFZ had significant microsegregation near the solidified grain boundaries (SGBs). The metallurgical heterogeneity in the WFZ caused the formation of localized stress zones, which directly affected the mechanical behavior of the WFZ. The carbide particles influenced the microhardness in the WFZ and P91 HAZ regions. The PWHT successfully homogenized the microhardness in the WFZ and P91 HAZ regions. The impact toughness decreased to 64 J from 82 J after PWHT due to precipitation at SGBs and its coarsening. The SMAW process involves multiple thermal cycles during welding. The deposition of filler metal in multiple welding passes created uncontrolled variations in the solidification behavior of the WFZ. Microsegregation had a detrimental impact on the microstructure and mechanical properties of the P91 and IN 800HT dissimilar metal welds.

https://doi.org/10.29391/2024.103.025

Keywords

- Microstructure
- Dissimilar
- Shielded Metal Arc Welding
- P91
- IN 800HT

Introduction

Given climate change, the International Energy Agency (IEA) produces data for average CO_2 emissions in electricity generation for advanced economies. The data shows a reduction of around 45% from 1990 to 2020 (Ref. 1). To further make improvements in the reduction of carbon emissions, advanced ultra-supercritical (AUSC-Generation IV) reactor-based power plants are options for reducing climate change. They can run at temperatures and pressures above the critical and supercritical range of the steam to increase overall output efficiency. The increase in efficiency directly subsides the CO_2 emissions (Ref. 2). The power plants focus on the design and selection of high-performance structural and component materials. Such materials are put to critical working conditions before their employment in service to increase the efficiency of the power plant and reduce in-service failures. The heat exchanger has components made up of P91 steel and Incoloy 800HT® (IN 800HT) (Refs. 3, 4). Welding these two materials is preferred to limit assembly components and cost. Apart from P91 and IN 800HT, many other dissimilar metal welds (DMWs) are also present in a power plant for better design considerations. P91 offers high strength and high-temperature resistance, while IN 800HT offers high-temperature applications, corrosion resistance, and better impact toughness.

Power plants often use ferritic-martensitic P91 steel and austenitic IN 800HT as structural materials. P91 steel can withstand temperatures of around 620°C and is cost-effective, while IN 800HT can endure temperatures of around 650°C and is resistant to corrosion. The gas tungsten arc

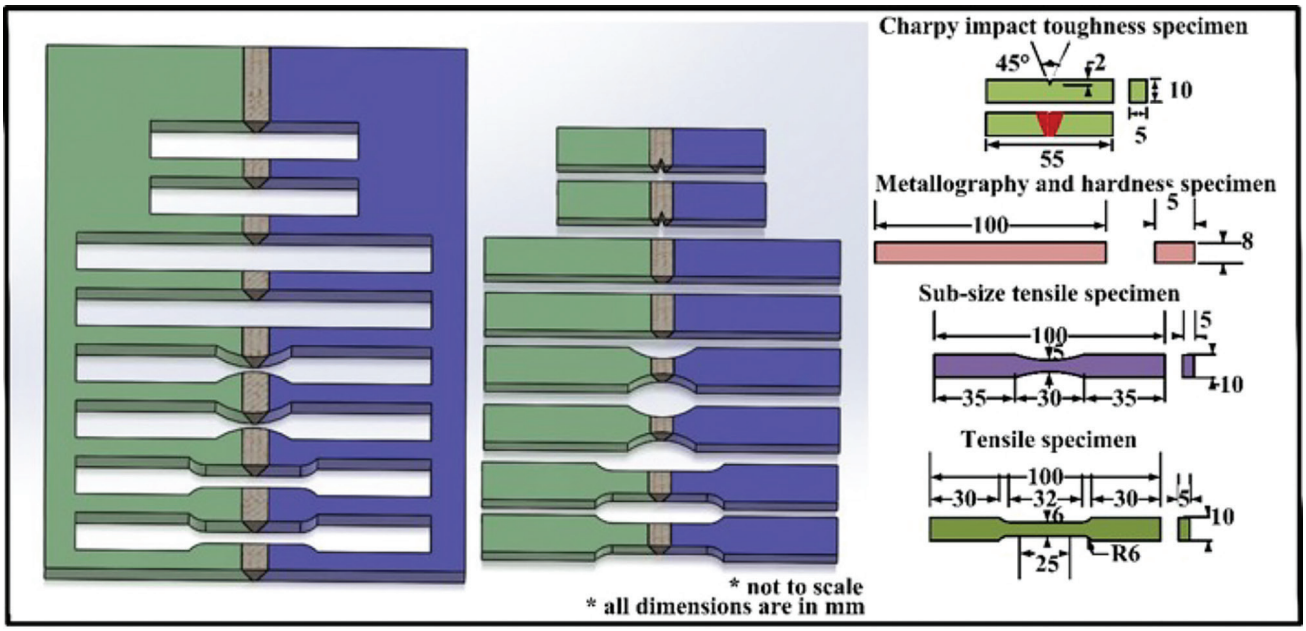

Fig. 1 — Schematic of specimen extraction scheme on wire-EDM and their dimensions.

welding (GTAW), high-energy density welding, and shielded metal arc welding (SMAW) processes are used widely to fabricate such DMWs (Refs. 5, 6). GTAW is preferred to provide greater control over heat input. The P91 and IN 800HT dissimilar metals weld using ERNiCr-3 filler through GTAW, obtaining a maximum UTS of 650 MPa and impact toughness of 86 J at room temperature in the as-welded (AW) specimen (Ref. 7). Using GTAW with ERNiCrCoMo-1 filler, the dissimilar metal weld between P91 and IN 800HT gave optimum weld strength with impact toughness of 117 J in the AW state and 102 J in a postweld heat treatment (PWHT) state (Ref. 8). The mismatch-related failures involving mechanical properties mismatched between base metal and filler and mismatched in coefficient of thermal expansion are detrimental. Mismatch in filler selection may also raise corrosion susceptibility by creating galvanic corrosion cells. SMAW is known for its on-site applications since its setup is simple, and the process is cheap and efficient. Kim et al. (Ref. 9) studied the SMAW joint of P91 steel using the E9016-G electrode and found that the heat-affected zone (HAZ) formed was highly prone to creep failure. Divya et al. (Ref. 10) studied the influence of welding processes on Type IV cracking in P91 steel and found no significant effect on creep life by decreasing the HAZ's width through advanced welding processes like electron beam welding (EBW) and laser beam welding (LBW). Ren et al. (Ref. 11) raised the concern of premature failure in DMWs during service life. Albert et al. (Ref. 12) also suggested that larger grain size in the HAZ could be the reason for improving creep strength in high-Cr steel, like P91. The formation of unwanted phases, creep cracking, stress corrosion cracking, undesirable microsegregation, and local strength mismatch can cause the failure of DMWs. Sometimes interlayers are used to bridge the material properties (Ref. 13).

IN 800HT is susceptible to intergranular cracking due to sulphidation-oxidation corrosion at elevated temperatures (Ref. 14). The material has a higher creep strength at high temperatures than IN 800H but can still degrade over time under exposure to elevated temperatures. P91 steel also degrades rapidly under thermal aging due to the coarsening of precipitates and the formation of Laves phases and modified Z phases (Ref. 15). A common cause of failure in dissimilar metal welds is the mismatch in the coefficient of thermal expansion between the materials (Ref. 16). To prevent this, interlayers that act as a transition between dissimilar metals and reduce carbon diffusion activity at the weld interface have been used. Also, nickel-iron-chromium alloys like IN 800HT are prone to microsegregation in the weld fusion zone, which can lead to harmful secondary intermetallic phases (Ref. 17). A lot of work has been reported on creep life analysis on SMAW welds, but a study of dissimilar welds of IN 800HT has not yet been reported.

The present study emphasizes the impact of employing multiple weld passes during the SMAW process, resulting in unregulated variations in the solidification characteristics of the weld fusion zone. This analysis highlights the significance of effectively managing the welding parameters and comprehending their influence on the development of microstructure. Additionally, the investigation examines the influence of postweld heat treatment. The study focuses on understanding the microstructural failures that can occur in Ni-based DMWs and aims to improve the strength of DMWs using advanced characterization techniques such as field emission scanning electron microscopy (FE-SEM) and energy-dispersive x-ray spectroscopy (EDS). The study also examines the mechanical properties of DMWs, including tensile strength, microhardness, and impact toughness. The goal is to establish a structure-property relationship for DMWs and contribute to the better development of DMWs for future power plant applications involving P91 steel and IN 800HT.

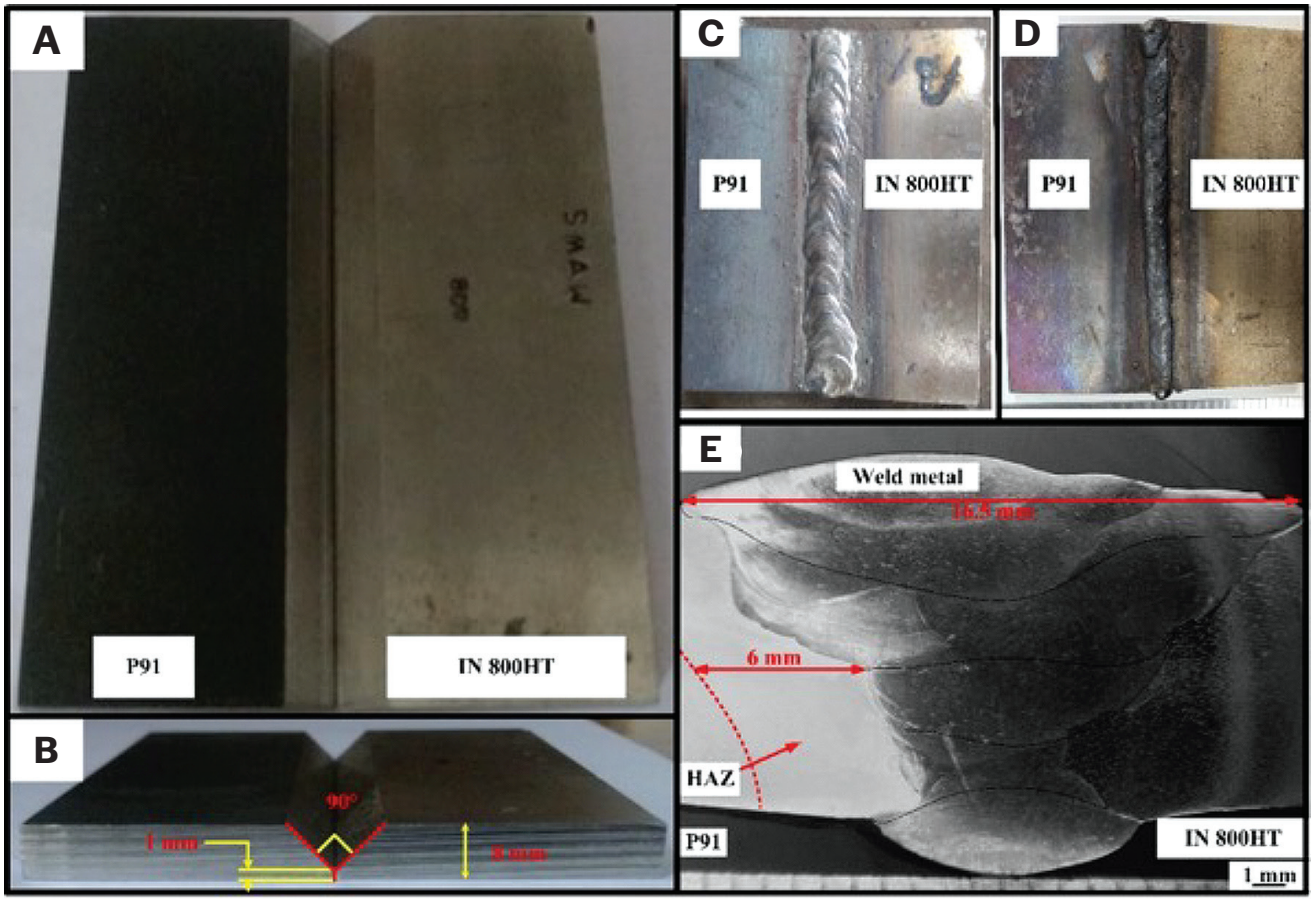

Fig. 2 — A — Machined groove surfaces; B — groove design schematic; C — welded plate top face; D — welded plate bottom face; E — SMAW weld macrostructure.

Table 1 — Elemental Composition of Base Metals in As-Received Condition

Elements (wt-%)	C	Ni	Mn	Mo	Ti	Al	Cr	Nb	Fe	Co	Rest
P91	0.09	0.3	0.4	1.0	0.002	0.01	8.4	0.07	88.8	—	0.84
IN 800HT	0.08	32.7	1.0	0.1	0.5	0.4	21.1	0.03	43.4	—	0.69
ENiCrCo-Mo-1	0.07	50.0	2.0	8.9	—	—	24.9	Nb + Ta = 0.7	2.1	11.0	0.33

Materials and Experiments

The study utilized P91 and IN 800HT as the materials being investigated. IN 800HT underwent a solution-annealing process, while P91 was obtained in a normalized and tempered condition. The normalization was performed at 1040°C for 40 minutes, and then the materials were air cooled. Tempering was done at 760°C, the holding time was two hours, and then the materials were air cooled. The elemental composition of the base metals was determined using optical emission spectroscopy, and the results are shown in Table 1. The observed average grain size of P91 grains was 16 ± 3 μm and 163 ± 18 μm for IN 800HT. The grain size measurement was done employing the intercept counting method. The mechanical properties observed for the base metals at room temperature (RT) are mentioned in Table 2.

The P91 plate was prepared and extracted on wire-EDM (electrical discharge machining) in 100 mm × 50 mm × 8 mm dimensions. Similarly, a plate was extracted from IN 800HT of the same dimensions. The surfaces of the extracted plates were prepared on a surface grinder to remove any oxide layer and foreign particles. The plates were butt welded in a flat

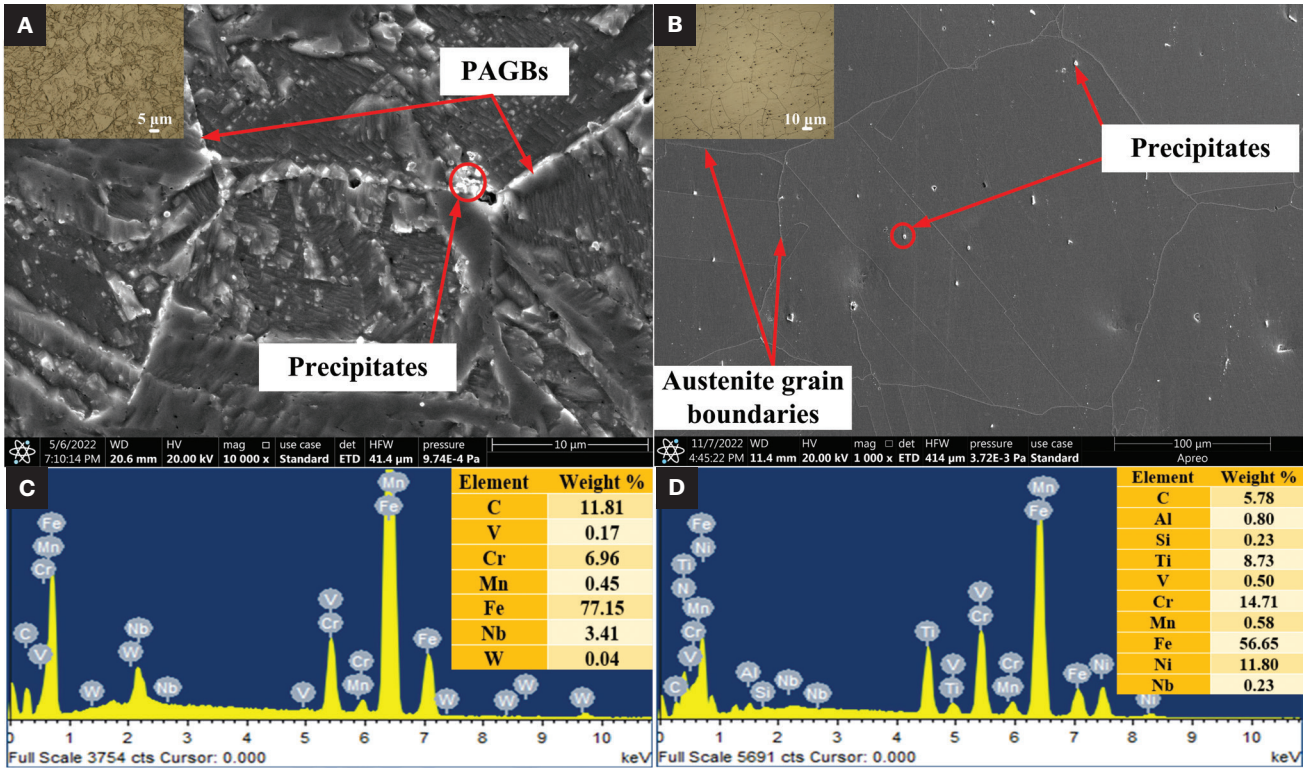

Fig. 3 — Micrographs and EDS spectrum of base metals: A — P91 microstructure; B — IN 800HT microstructure; C — elemental composition of circled P91 precipitates; D — elemental composition of circled IN 800HT precipitates.

Table 2 — Mechanical Properties Observed for P91 and IN 800HT Base Metals

Properties (at Room Temperature)	P91	IN 800HT
Bulk Microhardness	245 ± 15 HV	159 ± 20 HV
Impact Toughness	102 ± 4 J	110 ± 5 J
Ultimate Tensile Strength (UTS)	673 ± 8 MPa	593 ± 5 MPa
Yield Strength (YS)	445 ± 6 MPa	285 ± 4 MPa
Elongation %	22 ± 3	23 ± 3
Reduction in Area %	69 ± 3	65 ± 3

1(G) position using ENiCrCoMo-1 welding electrodes 3.2 mm in diameter. The welding was performed manually on a SMAW setup. The first root pass was made at parameters of 80 A and 16 V (arc voltage). The four filling passes were performed at 85 A and an average arc voltage of 20.6 V. A total of five passes were made with an average heat input of 0.8 kJ/mm. The average travel speed was 125 mm/min. The welding samples were extracted as per the schematic shown in Fig. 1. The samples were heat-treated at 760°C for 2 h in a muffle furnace. Microstructural observation, chemical analysis, and phase detection in the weld fusion zone were conducted using various instruments, such as the Thermo Fisher Apreo S Low Vac FE-SEM, Zeiss Ultra Plus SEM, Shimadzu Electron Probe Micronalyzer, and the Rigaku x-ray diffractometer. For electron probe microanalysis (EPMA), thin, polished sections of weld interfaces and WFZs were coated with a 30 nm-thin layer of gold using a Leica EM ACE200 sample coater. SX Five software was utilized to generate x-rays by employing a LaB6 electron gun operating at a voltage of 15 kilovolts and a current of 50 nanoamperes. The sampling time was 1 ms per point. The electron backscattered diffraction (EBSD) analysis was performed with a step size of 0.1 μm and at 20 kV

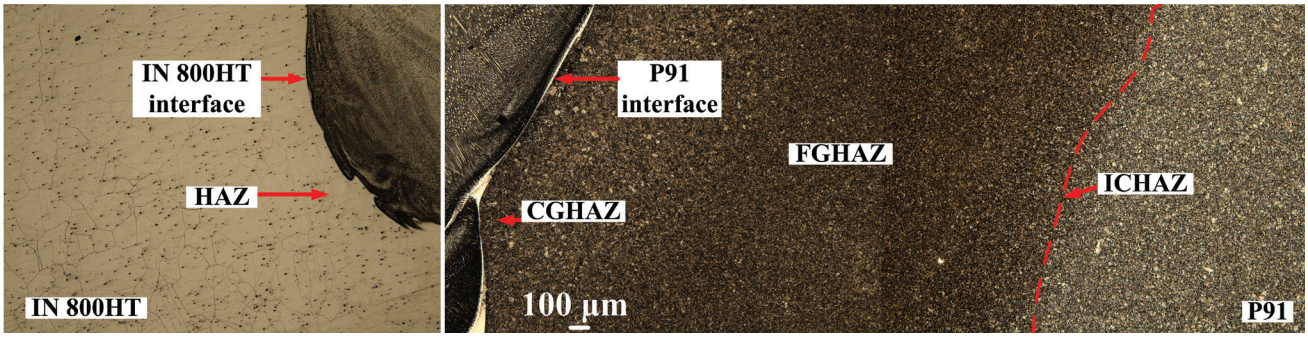

Fig. 4 — Stitched optical micrographs of the weld.

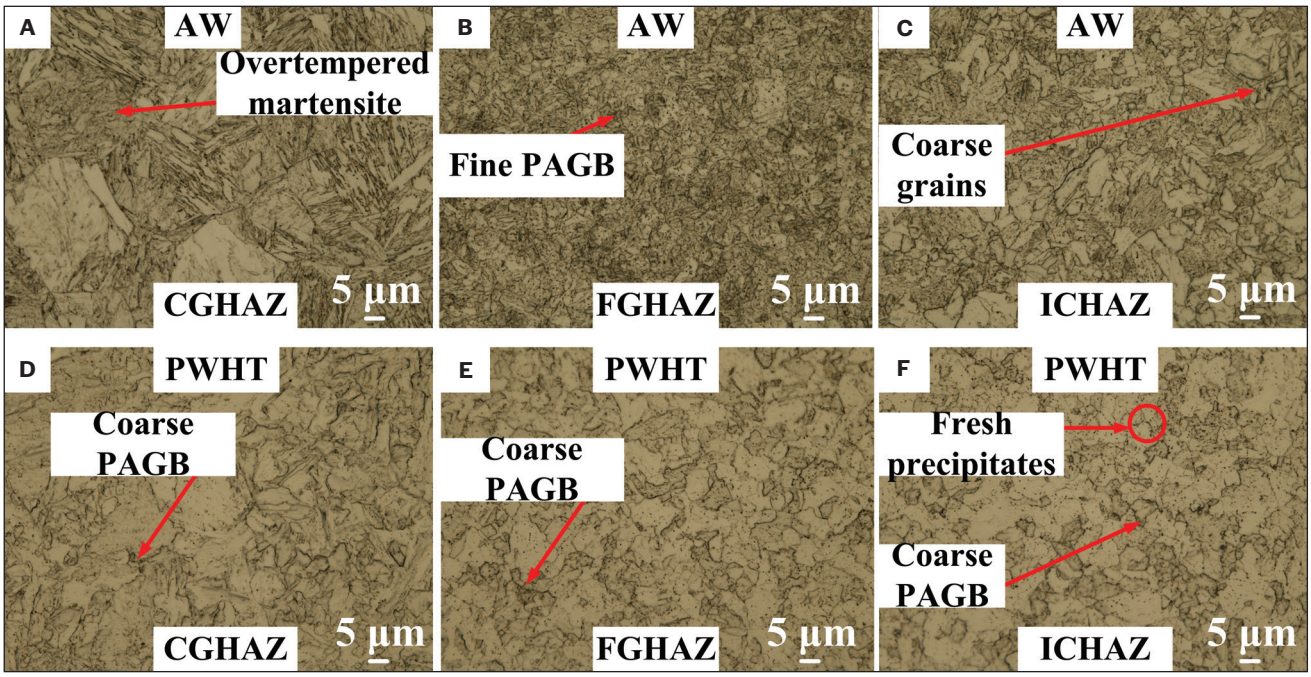

Fig. 5 — Optical micrographs of P91 HAZ: A — CGHAZ in AW state; B — FGHAZ in AW state; C — ICHAZ in AW state; D — CGHAZ in PWHT state; E — FGHAZ in PWHT state; F — ICHAZ in PWHT state.

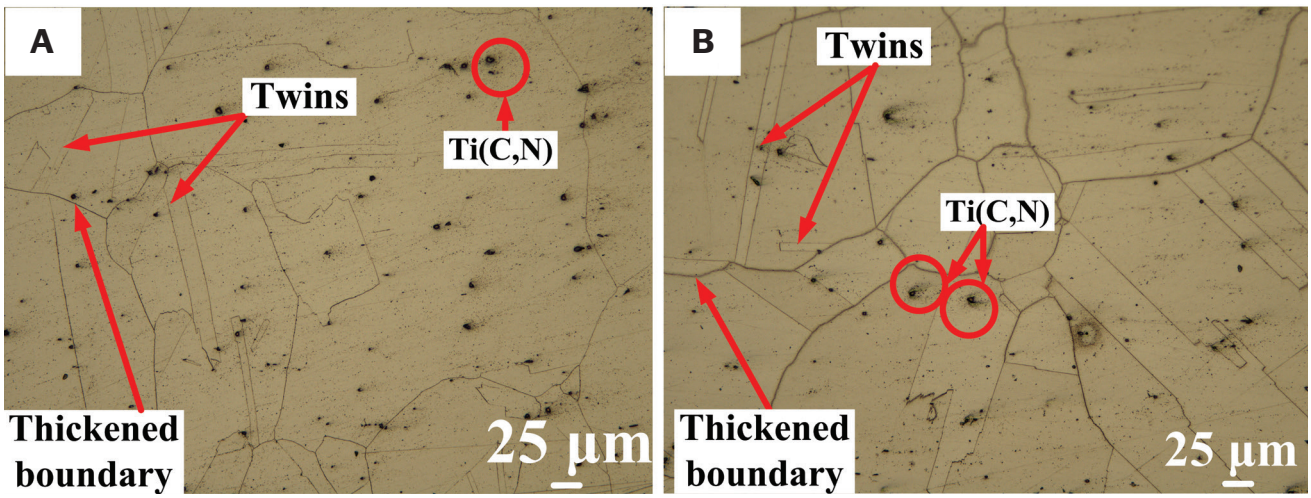

Fig. 6 — Optical micrographs of IN 800HT HAZ observed in: A — AW state; B — PWHT state.

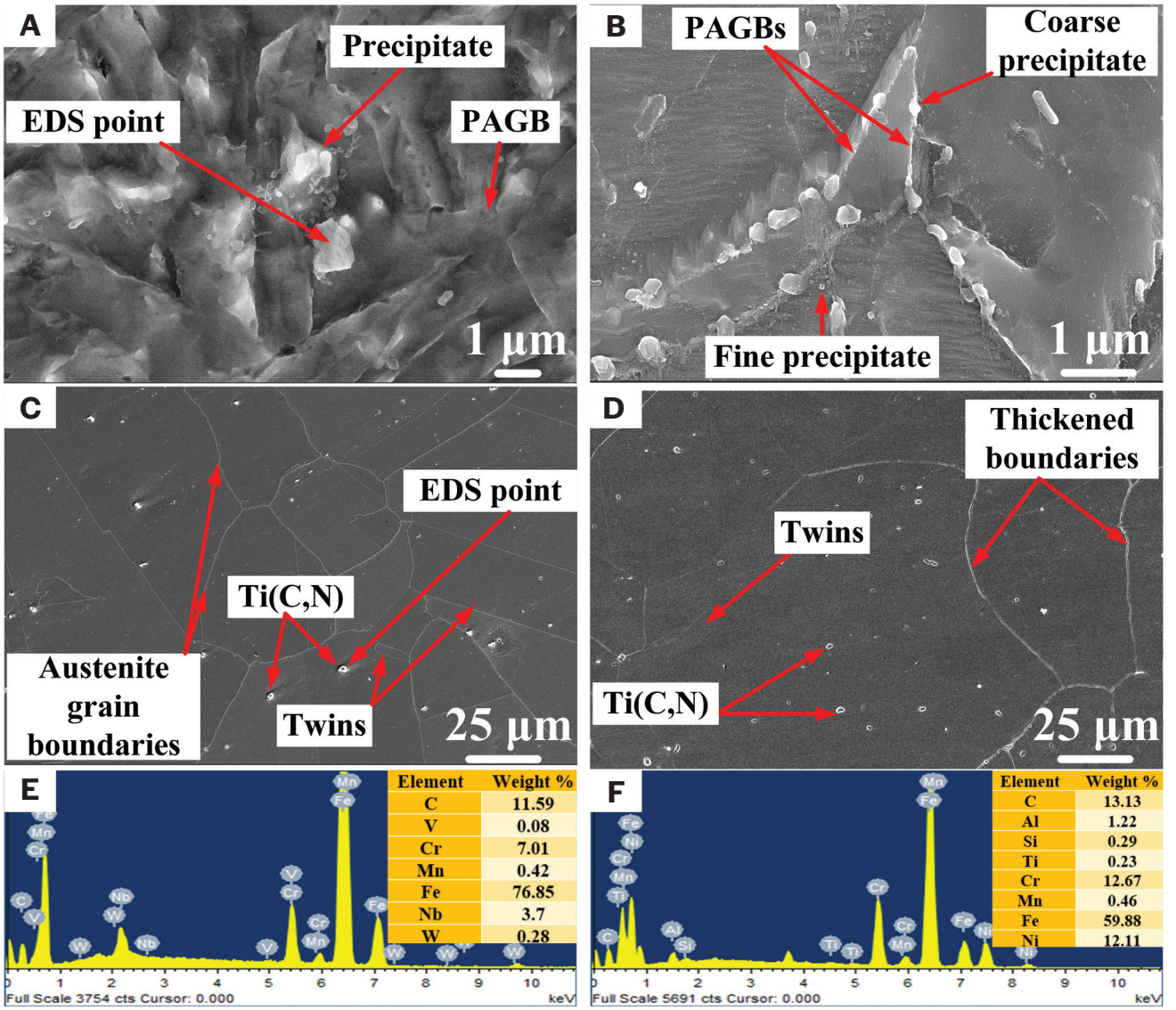

Fig. 7 — FE-SEM micrographs and EDS spectrum of: A — P91 CGHAZ in AW state; B — P91 CGHAZ in PWHT state; C — IN 800HT HAZ in observed AW-state specimen; D — IN 800HT HAZ observed in PWHT-state specimen; E — EDS spectrum of coarse precipitates in AW P91 CGHAZ; F — EDS spectrum of cuboidal precipitate in AW IN 800HT HAZ.

accelerating voltage to generate the EBSD patterns. TSL OIM software version 7.0 was used to analyze the acquired EBSD data. The impact toughness, tensile strength, and microhardness of the dissimilar metal weld were also tested using an Impact tester, universal tensile machine, and automatic Vickers microhardness tester. The indents were not taken near the specimen edges to prevent improper load distribution and were spaced at least 1 mm from the specimen edges. The indents in the transverse cross-section direction were taken at 0.5 kgf load and 0.5 mm apart to cover the narrower regions of the WFZ and HAZ. The rows of indents were also spaced at 0.5 mm apart. The specimens were prepared by manually polishing with emery papers and alumina slurry and etching using Vilella's reagent for the P91 specimen and 10% oxalic acid solution for IN 800HT.

Results

Microstructure Observations

The prepared groove and its design can be seen in Figures 2A and B. Figures 2C and D display the welded plate with a smooth weld bead. Figure 2E reveals the cross-section of the joint to show the weld bead and its depth of penetration. A macroexamination showed multiple welding passes without any visible flaws in the fusion zone or along the weld interfaces. The macrostructure also showed a 6 mm-wide P91 HAZ. Figure 3A reveals the P91 base metal's microstructure at higher magnification, which displays a martensitic structure with precipitates, lath packets, lath boundaries, and primary austenite grain boundaries (PAGBs). Figure 3B shows the IN 800HT's microstructure, which has larger grains of varying

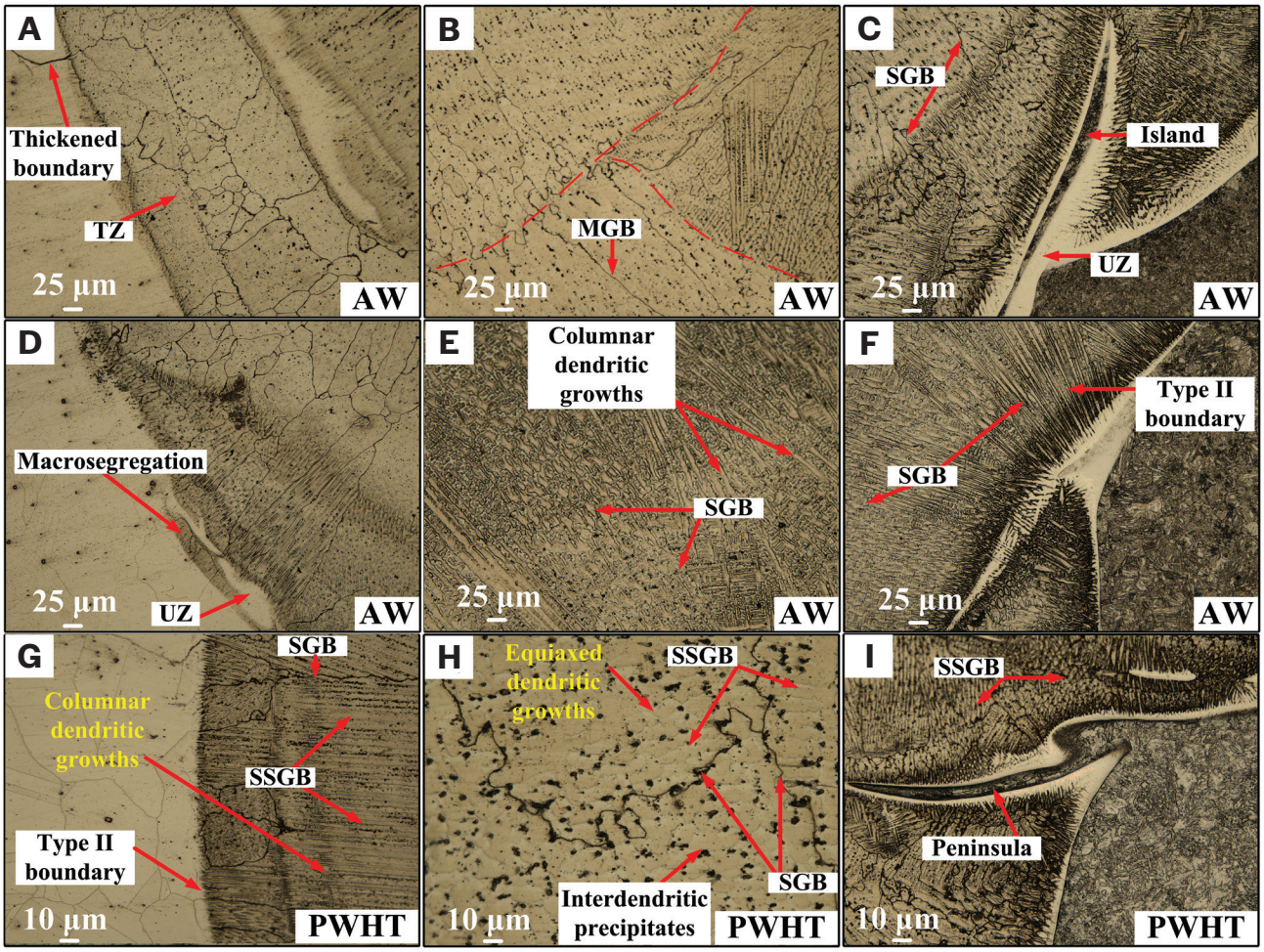

Fig. 8 — Optical micrographs of: A — IN 800HT weld interface (near weld top); B — WFZ (near weld top); C — P91 weld interface (near weld top); D — IN 800HT weld interface (near weld center); E — WFZ (near weld center); F — P91 weld interface (near weld center); G — IN 800HT weld interface (near weld root); H — WFZ (near weld root); I — P91 weld interface (near weld root).

size and abundant annealing twins and Ti-rich precipitates, contributing to its ductile nature. P91 has a body-centered cubic (BCC) structure, and IN 800HT has a face-centered cubic (FCC) structure. EDS spectra in Fig. 3C confirm the presence of Cr-rich carbide precipitates in the as-received P91 base metal's microstructure. Figure 3D shows the EDS spectrum of a circled cuboidal precipitate in the austenitic IN 800HT microstructure, which was identified as a Ti-based phase.

Figure 4 displays a stitched view of the P91 and IN 800HT welded joint under an optical microscope. The P91's HAZ is divided into three regions: coarse grain HAZ (CGHAZ), fine grain HAZ (FGHAZ), and intercritical HAZ (ICHAZ), as shown in Fig. 4. The IN 800HT HAZ did not show any grain size increase. The P91's HAZ experienced different transformation temperatures, with CGHAZ forming above Ac_3, FGHAZ slightly above Ac_3, and ICHAZ between Ac_1 and Ac_3 (Ref. 18). The P91's HAZ has the risk of Type IV cracking, and smaller grain size can significantly cause failure in the FGHAZ and ICHAZ regions of P91 (Ref. 19). FGHAZ and ICHAZ regions are exposed to high temperatures, which causes partial dissolution of secondary phase precipitates, as cooling after welding is too fast for complete dissolution (Ref. 20). It leads to failure as precipitate-forming elements are trapped, and fresh precipitation cannot occur during PWHT. Coarsening of undissolved precipitates during PWHT weakens the material and increases the risk of microcavity nucleation (Ref. 21). PWHT helps in rapidly precipitating second-phase particles ($M_{23}C_6$ and MX). Figures 5A–C show the HAZ regions in the as-welded state. The ICHAZ and FGHAZ had an average grain size of 18 ± 8 μm and 14 ± 5 μm, respectively, compared to 18 ± 10 μm in the P91 base metal. Figure 5C shows the CGHAZ with an average grain size of 36 ± 12 μm. Figures 5D–F show the changes in the HAZ region after PWHT.

Figure 6A shows the IN 800HT HAZ as observed in the AW-state specimen, and Fig. 6B shows the IN 800HT in the PWHT-state specimen. No substantial differences were noticed in the grain size of the IN 800HT's HAZ region, with an average size of 162 ± 15 μm before and after PWHT, while the IN 800HT base metal's average grain size was 163 ± 15 μm. The austenitic grain boundaries near the weld interface of IN 800HT were seen to be strengthened due to Ti deposition (Ref. 22). The IN 800HT's HAZ was also observed with M23C6 precipitates over the grain boundaries due to PWHT. The austenitic grains were well-distributed with annealing twins.

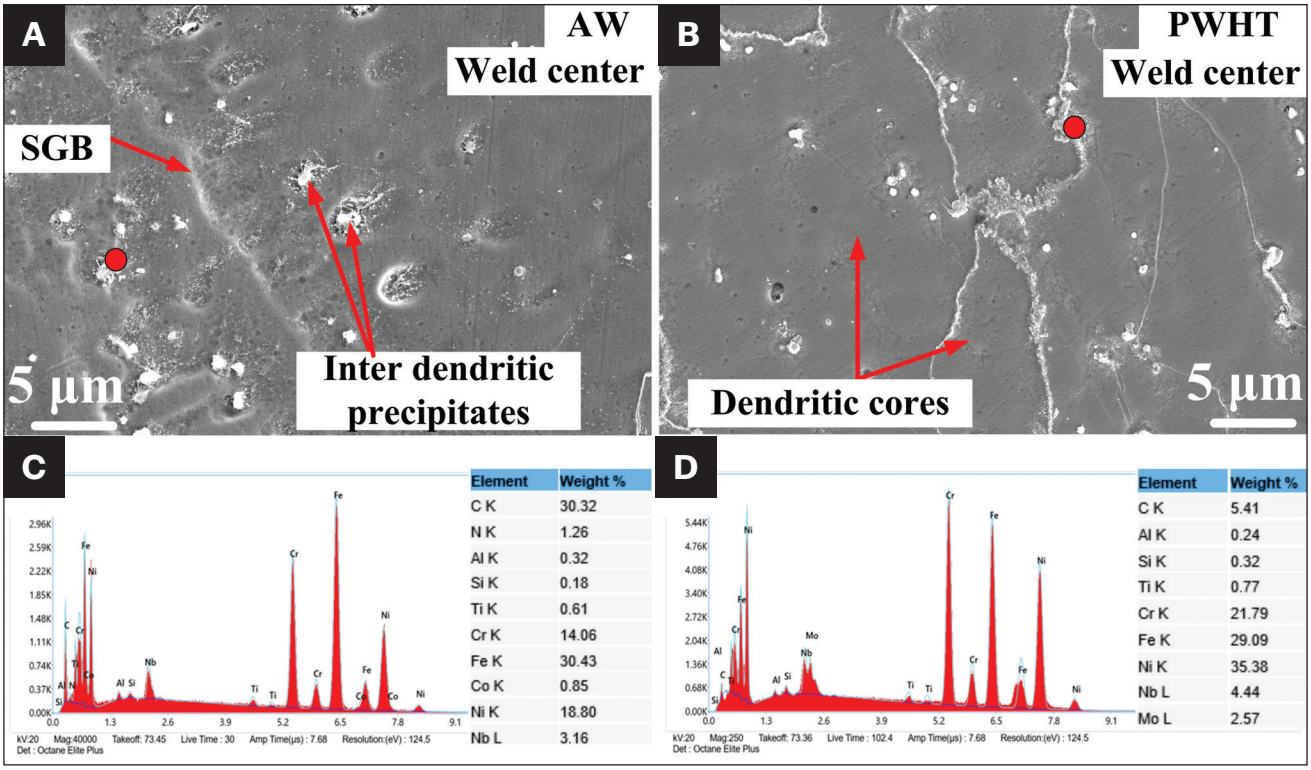

Fig. 9 — FE-SEM micrograph and EDS spectrum of: A — WFZ in AW state; B — WFZ in PWHT state; C — spotted interdendritic particles in AW states WFZ; D — spotted interdendritic particles in PWHT states WFZ.

Table 3 — Segregation Coefficient and Elemental Composition of Different Structures Investigated in the WFZ.

Spectrum	Position	C	Cr	Fe	Co	Ni	Nb	Mo
EDS (wt-%)	Dendritic Core (C_S)	30.67	16.93	6.23	7.45	31.90	3.01	3.81
	Interdendritic Region (C_L)	32.32	17.21	5.11	7.33	30.66	3.16	4.21
	Segregation Coefficient k	0.9	0.9	1.2	1.01	1.04	0.9	0.9

Figures 7A and B show the FE-SEM micrographs of the P91's CGHAZ in the as-welded and postweld heat-treated states. The exposure to higher temperatures in the CGHAZ region caused the complete dissolution of precipitates, reducing their ability to anchor the PAGBs and causing an increase in grain size. After heat treatment, heavy concentrations of newly formed and coarse precipitates were observed in the CGHAZ matrix and PAGB. Figure 7E shows the EDS spectrum of a precipitated particle after PWHT, indicating it was C-rich and Cr-based, and later, the same was confirmed in the EPMA results. Figures 7C and D show the FE-SEM micrographs of IN 800HT HAZ in the as-welded and postweld heat-treated states. Figure 7F shows the EDS spectrum of a cuboidal particle in the IN 800HT's HAZ; peaks of Ni, Al, Ti, and Cr can be contemplated for the presence of either the TiC or γ' phase. Annealing twins were also observed in the microstructure.

The light optical microscopic images in Figs. 8A–F show the AW state specimen, while Figs. 8G–I show the PWHT state specimen. Figures 8A–C display the P91 weld interface, WFZ, and IN 800HT weld interface, respectively, from the top of the weld. Figures 8D–F show the same interfaces from the center of the weld. The optical analysis of the P91 weld interface showed the presence of macrosegregation in the form of peninsulas and islands. The IN 800HT weld interface had extensive austenitic grain growth near the weld interface. Some regions of the IN 800HT weld interface near the center region had the formation of a transition zone and a Type II boundary. A Type II boundary denotes a distinct grain boundary that emerges amidst columnar grains during

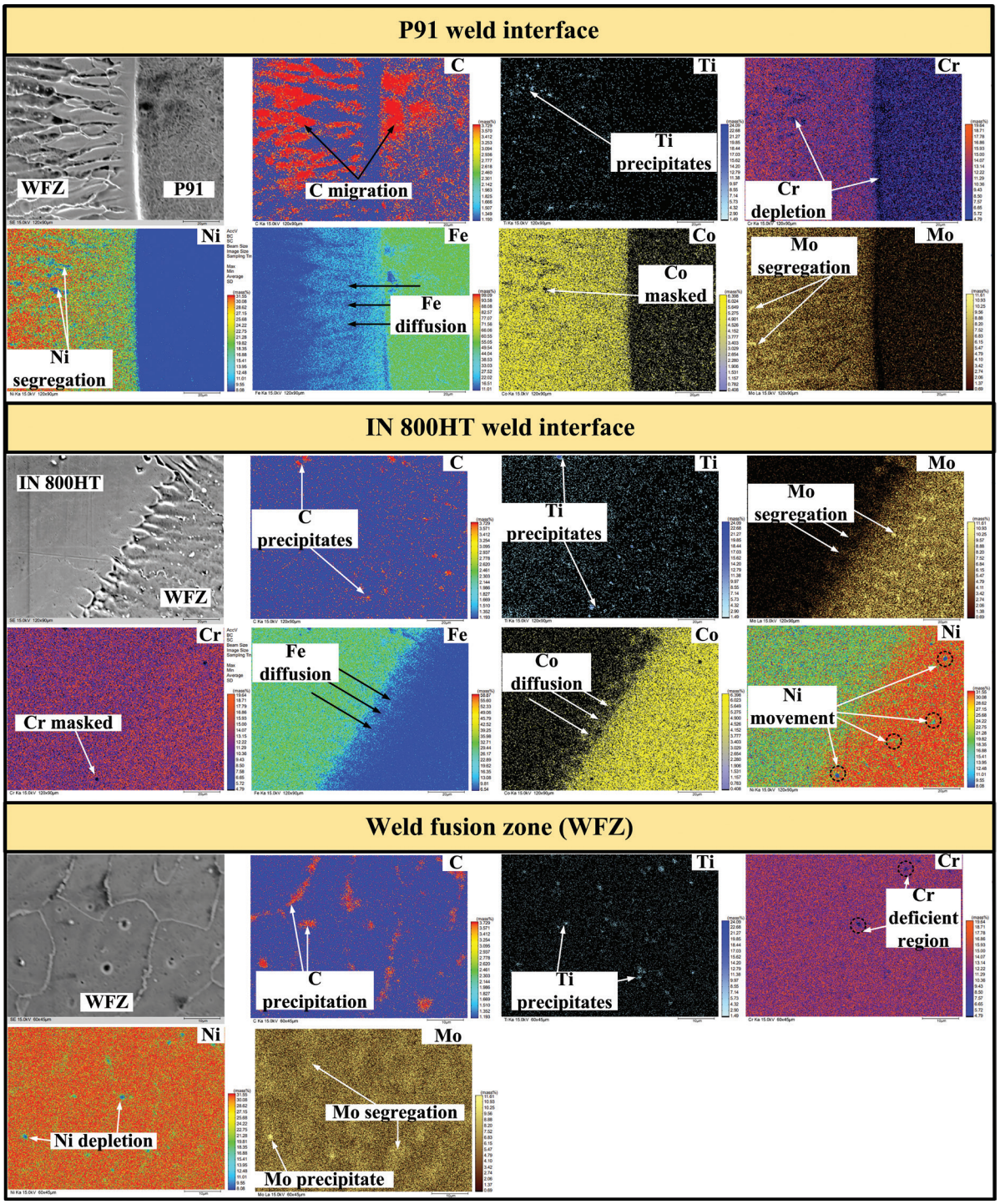

Fig. 10 — EPMA qualitative analysis of P91 weld interface, IN 800HT weld interface, and WFZ.

solidification. The IN 800HT weld interface near the top of the weld had thicker transition zones and an unmixed zone. In the center of the weld were columnar dendritic growth at the interface and well-extended austenitic grain boundaries. Near the weld root, a Type II boundary was formed. This variation in the interface was due to different solidification rates from multiple weld passes. The WFZ had randomly distributed columnar and equiaxed dendritic patches. Solidified grain boundaries, solidified sub-grain boundaries (SSGBs), and migrating grain boundaries (MGBs) were also present. The cells or dendrites exhibited distinct boundaries. This differentiation can be attributed to the redistribution of solutes, commonly referred to as the SSGB. The boundary formed by the intersection of sub-grains or cells within a similar group can be referred to as a solidified grain boundary (SGB). SGBs and SSGBs form as the liquid film between two grains and dendrites solidify last, respectively. Simultaneously, a grain boundary with a high-angle misorientation, where the crys-

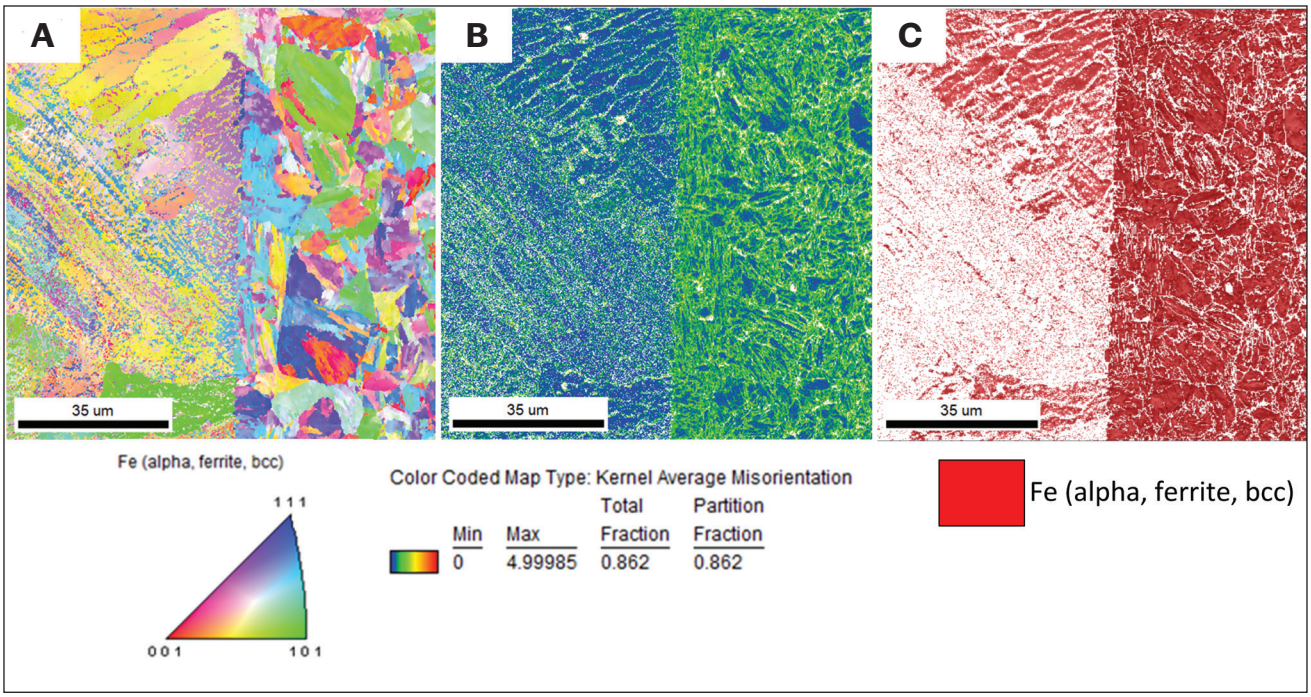

Fig. 11 — EBSD scan at P91 weld interface: A — IPF map; B — KAM map; C — phase map.

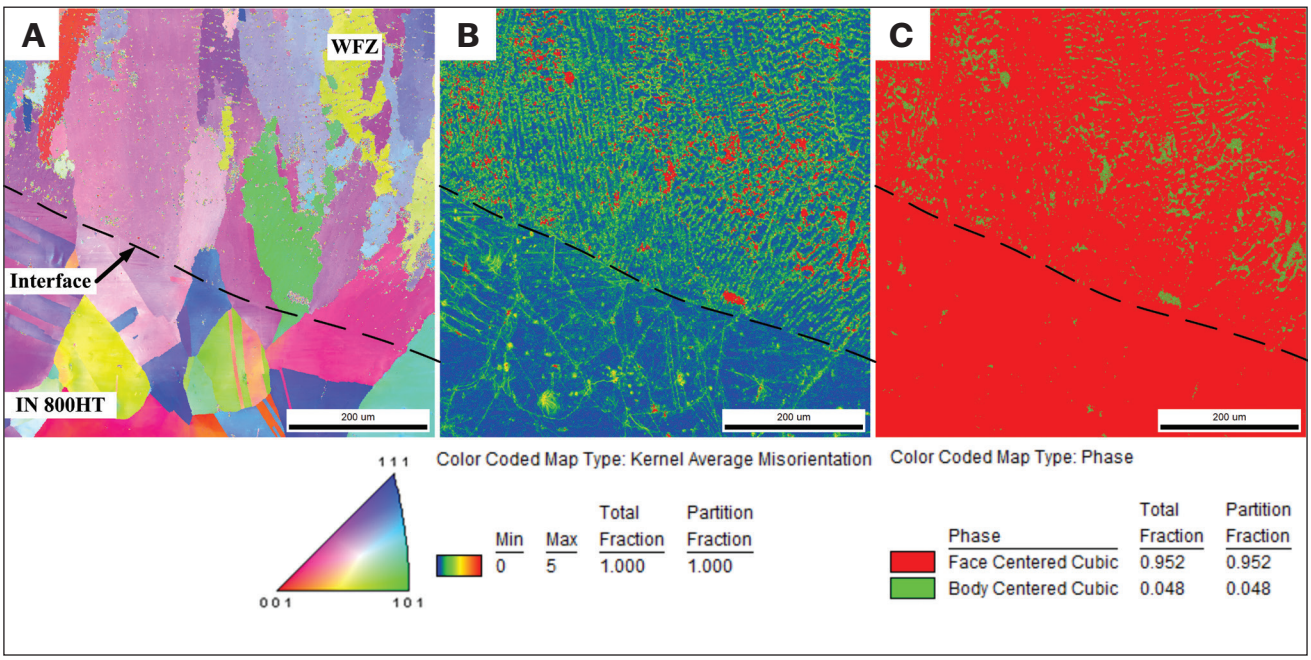

Fig. 12 — EBSD scan at IN 800HT weld interface: A — IPF map; B — KAM map; C — phase map.

tallographic component moves apart from its compositional component, can be referred to as a MGB. MGBs formed due to rapid solidification in some regions of the WFZ.

Figures 9A and B show the WFZ in the AW and PWHT states. The columnar dendritic regions in the AW and PWHT states were observed with SSGBs, SGB, interdendritic particles, and dendritic cores. The EDS spectrum in Fig. 9C confirms the presence of C-rich phases in the interdendritic region of the WFZ, while the interdendritic regions show Ti diffused into a liquid phase during solidification (Ref. 23). Figure 9D shows high C deposition in the interdendritic region after PWHT.

The FCC crystal structure of Ni-based alloys leads to slower diffusion rates of alloying elements, causing microsegregation during welding solidification (Ref. 24). Table 3 presents the elemental compositions in the dendritic core and interdendritic region. The PWHT sample was examined using EDS

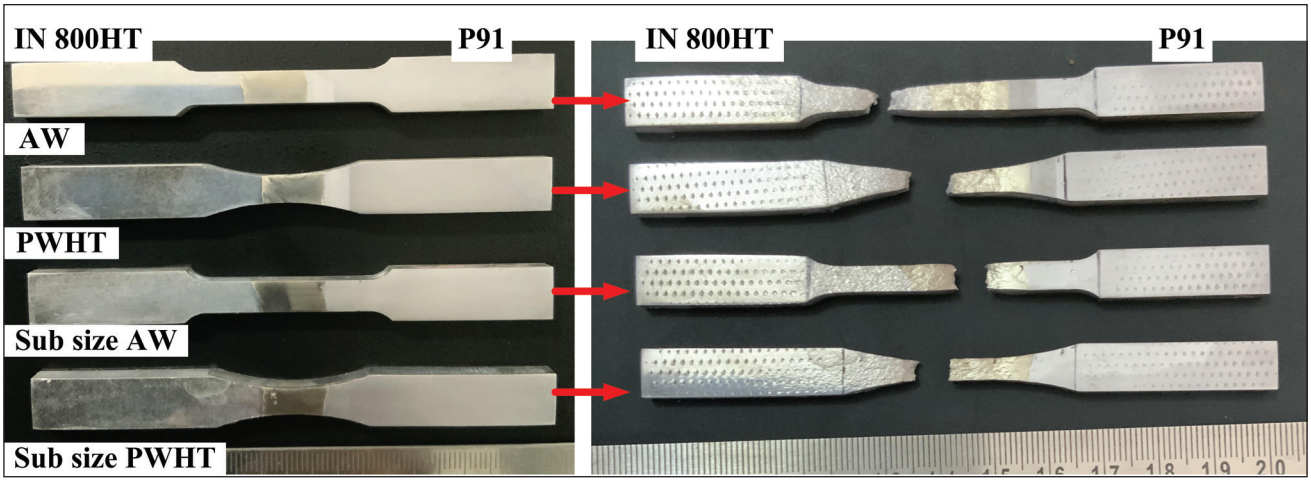

Fig. 13 — Prepared tensile specimens and fractured tensile specimens after testing.

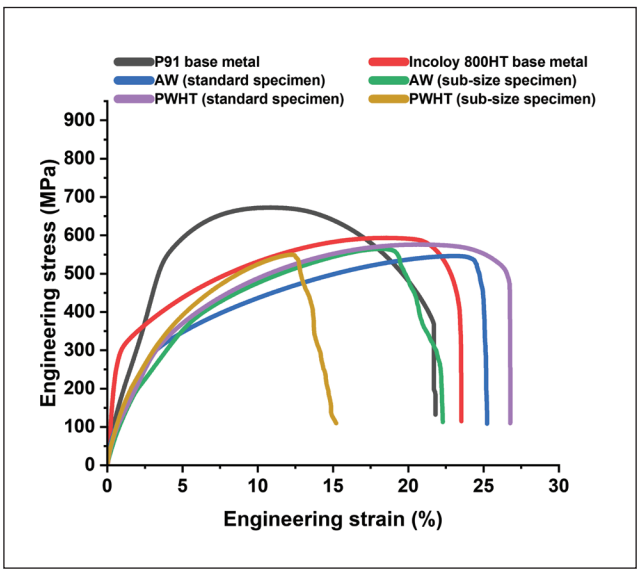

Fig. 14 — Plotted engineering stress-strain curves for base metals and tested tensile specimens.

to measure the elemental compositions in the WFZ's dendritic cores and interdendritic regions. Segregation coefficients were calculated from the EDS data by using Equation 1 (Ref. 25). Fe, Co, and Ni segregation coefficients were greater than 1, indicating that these elements were present in the solidified dendritic core (solid phase). The results of the EDS analysis showed that while Ni did not significantly segregate during solidification, elements such as C, Cr, Nb, and Mo were found to have segregated into the interdendritic region of the WFZ. Nb was mainly seen to concentrate in the interdendritic region. Cr segregation led to the formation of carbides, which could have harmed the material's mechanical properties. C segregation also had a negative effect. Also, cooling and reheating during the multipass welds promoted the change in composition. The segregation coefficient k, calculated as the ratio of the average element concentration of the alloying elements in the dendritic core and interdendritic region of the WFZ, determined the extent of segregation of the alloying elements.

$$\text{Segregation coefficient } k = \frac{C_S(\text{Solid})}{C_L(\text{Liquid})} \quad (1)$$

EPMA was conducted to examine diffusion and segregation at the weld interfaces and nearby solidified WFZ regions. Figure 10 shows the EPMA results for the P91 weld interface. The WFZ was enriched with C, likely resulting from different carbide formations (Mo, Ti, Cr-based). Heavy carbon segregation was seen in the interdendritic region of the WFZ near the P91 weld interface. Depletion of Cr was noticed in the P91's HAZ near the weld interface, while Fe diffusion into the weld fusion zone was evident. Mo and Ni segregation near the dendritic region was also seen. Co showed no segregation activity. Figure 10 shows the EPMA results for the IN 800HT weld interface. The C-deposited region suggests a C-rich precipitate, but no heavy carbon segregation was observed. Ti-rich precipitates were evenly distributed.

Cr was slightly high in the WFZ near the IN 800HT weld interface, and Fe concentration was higher in the WFZ due to diffusion. Ni movement was restricted near the IN 800HT region since the WFZ had a higher Ni composition. Mo was found to be segregated near the columnar dendritic region in the WFZ because of multiple thermal cycles during the welding deposition. Variation in Co composition from the WFZ to the IN 800HT's HAZ was seen and may have been due to diffusion activity in the transition zone at the weld interface while in a partially melted state. Further, the EPMA scan for the WFZ in Fig. 10 shows an evident deposition of C over SGBs and a heavy presence of Ti-rich precipitates in the WFZ. Mo segregation was also witnessed in the dendritic cores, detrimental to the mechanical properties. Ni depletion was also observed over the SGBs in the WFZ.

The Electron Backscatter Diffraction (EBSD) scan (Fig. 11) showed random orientation of the P91's HAZ grain near the P91's weld interface in the WFZ. The inverse pole figure (IPF) map (Fig. 11A) showed different orientations of the dendritic groups in the WFZ. The kernel average misorientation (KAM) map (Fig. 11B) indicated high levels of local strain in the P91's

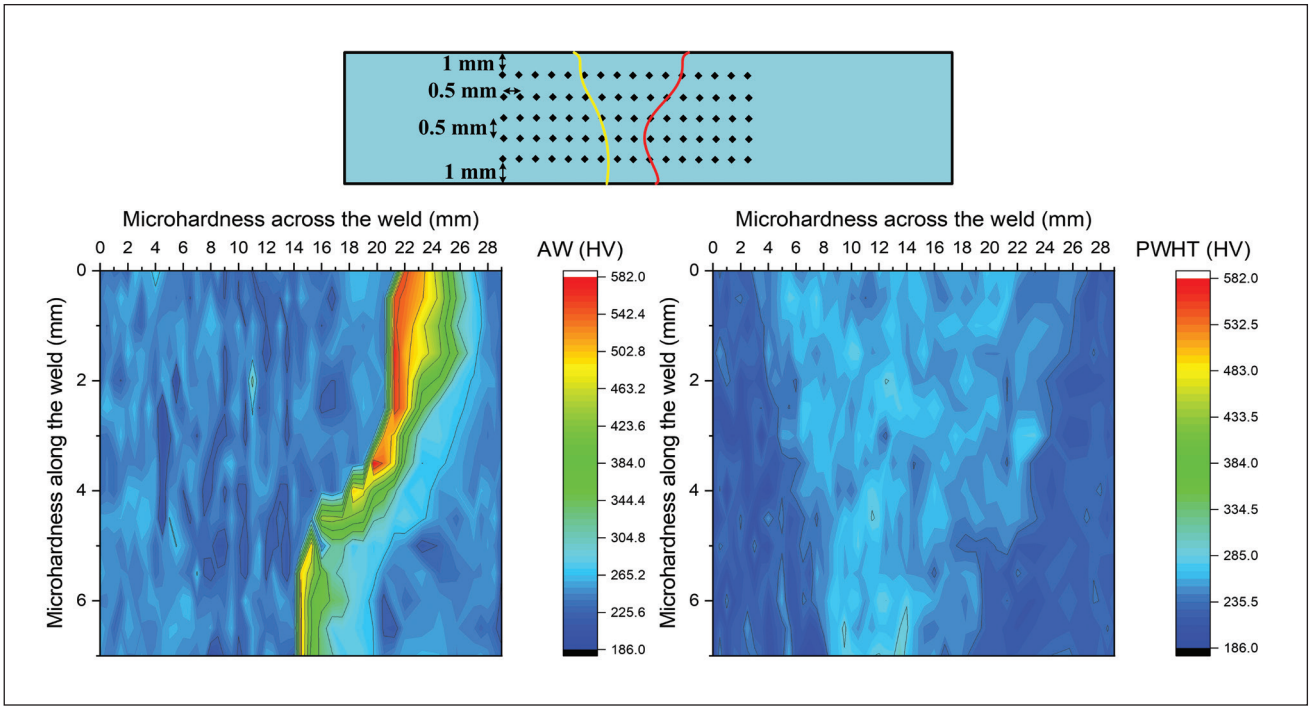

Fig. 15 — 2D contour profile plot of microhardness across the specimen in AW and PWHT states.

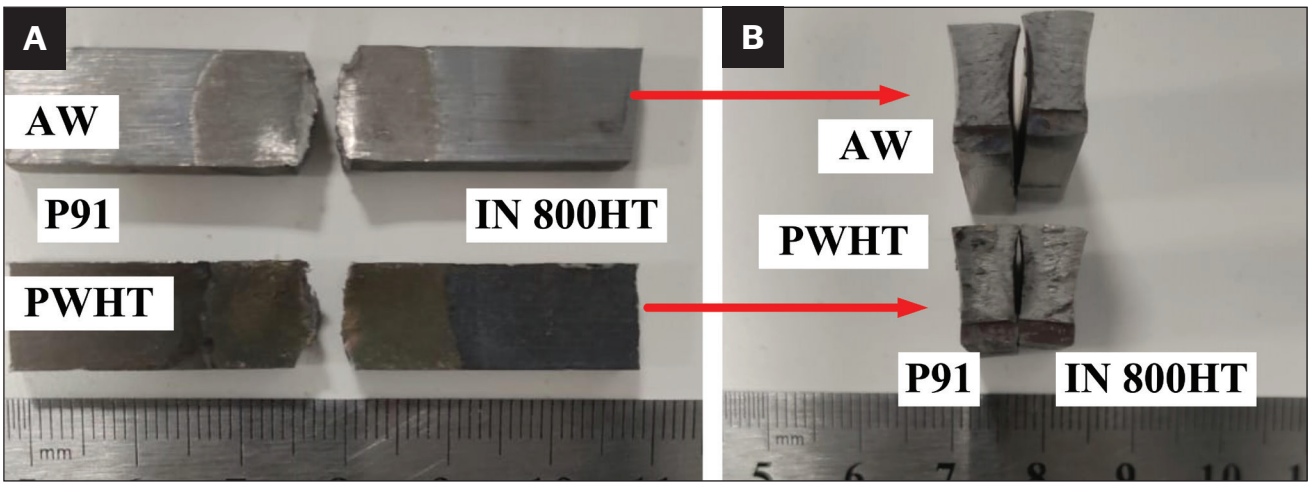

Fig. 16 — V-notched Charpy impact toughness specimens: A — After fracture; B — fractured tips.

HAZ and uneven distribution in the WFZ. In the EBSD scan (Fig. 12) for the IN 800HT's weld interface, the IPF map (Fig. 12A) showed the random orientation of grains, and the KAM map (Fig. 12B) revealed high levels of dislocations and strains in the WFZ compared to the HAZ regions. The phase maps indicated the presence of BCC crystal structure (Fig. 11C) in the P91's HAZ and FCC crystal structure (Fig. 12C) in the IN 800HT and WFZ. The IN 800HT's weld interface had extensive grain growth into the WFZ, indicating epitaxial growth near the weld interface. In comparison, the P91's weld interface was distinguished, and dendritic growth in varied orientations was observed at the weld interface. It could be inferred from the results that WFZ solidification was mostly austenitic. KAM showed an uneven distribution of dislocations across the weld interface, which makes the WFZ and HAZ regions highly prone to failure. In a similar study by Sakthivel et al. (Ref. 21), KAM showed higher strain distribution in the P91's HAZ region, contributing to the failure. In the present study, the quality of scans was not optimal, as significant noise was present in the WFZ because the samples were manually polished and the step size was 0.1 μm.

Mechanical Properties

The study examined the tensile strength of the welded joint in both the AW and PWHT states (Fig. 13). The tensile test results are summarized in Table 4. The AW- and PWHT-state standard specimens had ultimate tensile strengths

Table 4 — Tensile Properties of Different Weld Specimens

Specimens	UTS (MPa)	Ys [offset 0.2%] (MPa)	Elongation (%)	Reduction in the Area (%)	Failure Site
AW (Standard Specimen)	546 ± 5	197 ± 5	33 ± 2	52 ± 2	Base Metal IN 800HT
AW (Subsize Specimen)	561 ± 5	—	15 ± 2	11 ± 3	IN 800HT Weld Interface
PWHT (Standard Specimen)	576 ± 5	182 ± 6	27 ± 2	44 ± 3	WFZ
PWHT (Subsize Specimen)	540 ± 5	—	20 ± 3	12 ± 3	WFZ

(UTS) of 546 MPa and 576 MPa, respectively, and their yield strengths (YS) were 171 MPa and 123 MPa, respectively. The AW standard specimen failed from the IN 800HT base metal side, while the PWHT standard specimen failed from the weld fusion zone. The stress-strain curves are depicted in Fig. 14. The KAM map exhibits a significant strain distribution in the heat-affected zone (HAZ) of the P91 material. Consequently, it can be inferred that the failure originated from the region of the P91's HAZ. However, it is essential to note that the tensile strength of a material is influenced by various factors related to its microstructure, such as grain size, grain shape, grain boundary orientation, and other pertinent characteristics. The presence of segregated elements at the SGBs can lead to a notable degradation in mechanical strength.

In some cases, high KAM values can lead to improved tensile strength due to the presence of substructures, such as second-phase particles that reinforce the material and enhance its mechanical properties. In support of such exceptional behavior, few works of literature have reported that in nickel-based superalloys, failure occurred from the region where the high-stress concentration was observed in the EBSD KAM map (Refs. 26, 27).

Vickers microhardness tests were conducted on etched metallographic specimens, as shown in Fig. 16. The microhardness variation in a weld has been depicted using 2D contour plots created in OriginPro 2022b software. Figure 16 depicts the microhardness variation along and across the weld in the AW state, with the highest values in the CGHAZ region (582 HV) near the weld center. The values decreased gradually from the CGHAZ to ICHAZ and matched the base metal readings. The increase in microhardness in the FGHAZ (342 HV) and CGHAZ regions is attributed to the dissolution of precipitates. The ICHAZ had a minimum value of 199 HV. The WFZ HAD a uniform distribution with an average of 256 ± 15 HV. The IN 800HT'S HAZ in the AW state had an average microhardness of 243 ± 15 HV, and the base metal regions had an average of 238 ± 15 HV and 253 ± 15 HV for IN 800HT and P91, respectively. The contour profile across the weld shows a rise in microhardness in the P91's HAZ region and remains constant along the remaining region.

The 2D contour map of microhardness in the PWHT specimen is shown in Fig. 15. PWHT is known to temper the microstructure, re-evolve dissolved precipitates, and improve toughness (Ref. 28). The CGHAZ region was found to have a drastic reduction in microhardness to 268 ± 15 HV. The CGHAZ region above the weld center and near the top weld region was observed with a peak microhardness of 441 HV. The FGHAZ region also dropped to an average microhardness of 257 ± 20 HV. The ICHAZ region showed an increase in microhardness levels, with an average of 221 ± 10 HV. The resurfacing of carbide precipitates homogenized the P91's HAZ microhardness during tempering. In addition to the changes observed in the P91's HAZ region, the WFZ after PWHT also suffered a decline in microhardness. An average microhardness of 262 ± 15 HV was measured in the WFZ. The IN 800HT's HAZ and the base metal region also showed a drop in average microhardness to 235 ± 20 HV and 224 ± 15 HV, respectively. The reduction in microhardness can likely be attributed to the precipitation of the Cr-rich $M_{23}C_6$ phase, which occurs at the PWHT temperature of 760°C (Ref. 29). The microhardness at the P91 weld interface was 268 HV in the top weld region and 266 HV near the weld root region. While there was no significant variation along the IN 800HT's weld interface, the microhardness at the IN 800HT's weld interface in the PWHT state was 212 ± 5 HV.

The study conducted V-notched impact toughness tests on AW and PWHT specimens, as shown in Fig. 16. The impact tests were conducted as per ASTM E23, *Standard test methods for notched bar impact testing of metallic Mmaterials* (Ref. 30). The AW specimen had an average impact toughness value of 82 J and exhibited a ductile mode of failure with shear lips and lateral expansion of 2.5 mm. The PWHT specimen had a slightly lower average impact toughness value of 64 J. The slight increase in toughness in the PWHT specimen could be attributed to carbide precipitation in the WFZ that helped stabilize the grain boundaries and dislocations. Both specimens had lower impact toughness compared to the base metal toughness of P91 (102 J) and IN 800HT (110 J). The impact toughness of the weld met the standards set by EN ISO 3580:2017, *Welding Consumables*, and the American Society of Mechanical Engineers' boilers and pressure vessel code. The fractography micrographs (Figs. 16A and B)

showed a uniform distribution of dimples and cleavage facets, indicating a hybrid mode of failure that was predominantly ductile. The low impact toughness may have been caused by the formation of fusion centerline and columnar dendrites, which provide an easy path for fracture propagation. Studies by Sims et al. also suggest that the precipitation of $M_{23}C_6$ carbides can improve the mechanical properties of Ni-based alloys (Ref. 31).

Conclusion

The SMAW process was successfully used to study dissimilar metal welding between P91 and IN 800HT, and it was found to be suitable for use in Generation IV power plants. The following points can be deduced from the results obtained.

1. The dendritic growth on the P91 weld interface was in completely different orientations, but at the IN 800HT's weld interface, the growth of the austenitic grain was extended into the WFZ. Moreover, the growth near the IN 800HT weld interface was epitaxial.

2. The WFZ was witnessed with heavy carbide precipitation near the SGBs due to the deposition of multiple filler deposition passes made during welding, which enabled the redistribution of solute particles.

3. The IN 800HT's weakness was concluded to be due to Ti deposition near the grain boundaries of austenitic grain present adjacent to the IN 800HT's weld interface. It resulted in the thickening of the grain boundaries and possible intergranular failure in the region.

4. Microhardness varied immensely in the P91's HAZ region, with a peak value of 582 HV in the CGHAZ region of an AW-state specimen. The WFZ had an average distribution of 256 $\pm$ 15 HV. The microhardness in the IN 800HT's HAZ was around 243 $\pm$ 15 HV. PWHT was recommended for the tempering of the P91's HAZ region.

5. The microhardness contour plot showed uniform distribution in the weld fusion zone and variation in the P91's and IN 800HT's HAZs. The P91's HAZ showed increased microhardness in the as-welded state due to the partial dissolution of precipitates, while no significant changes were seen in the IN 800HT's HAZ. The impact toughness of the as-welded specimens in the weld fusion zone was 82 J, fulfilling EN standards.

Declaration of Competing Interest

The authors declare that they have no known competing financial interests or personal relationships that could have appeared to influence the work reported in this paper.

Acknowledgment

The authors would like to thank the Indian Institute of Technology Delhi (IIT Delhi) for providing the EPMA facility.

References

1. Cozzi, L., Gould, T., Bouckart, S., Crow, D., Kim, T. Y., and McGlade, C., et al. 2020. *World Energy Outlook 2020*. 2050: 213–50.

2. Siefert, J., Parker, J., and Totemeier, T. 2016. Complexities of in-service failures in dissimilar metal welds between Grade 91 and austenitic stainless steels. *ASME Pressure Vessels and Piping Conference* 5: 1–9. DOI: 10.1115/PVP2016-63982

3. Wojsyk, K., Golaski, G., Jasak, J., Sania, J., Zieliski, A., and Urbaczyk, P. 2016. Influence of the annealing time after welding on the mechanical properties of welded joint of T91 steel. *Archives of Metallurgy and Materials* 61: 1079–84. DOI: 10.1515/amm-2016-0233

4. Anand, K., Arun Kumar, S., Tamilmannan, K., Sathiya, P., and Arivazhagan, B. 2016. Metallurgical characterizations and mechanical properties on friction welding of Incoloy 800H joints. *Journal of Materials Research* 31: 2173–85. DOI: 10.1557/jmr.2016.161

5. Kotecki, D. J., Ogborn, J. S., İ SDR, ASM International, and Cavcar, M. M. *Sert Dolgu Alaşımları Ürün Seçimi ve Uygulama*, Oerlikon Kaynak Elektrodları ve Sanayi A.Ş., 1-31. ASM International 2019 74: 269–78.

6. DuPont, J. N. 2009. Welding metallurgy and weldability of nickel-base alloys. DOI: 10.1002/9780470500262

7. Bhanu, V., Pandey, C., and Gupta, A. 2022. Dissimilar joining of the martensitic grade P91 and Incoloy 800HT alloy for AUSC boiler application: Microstructure, mechanical properties and residual stresses. *CIRP Journal of Manufacturing Science Technology* 38: 560–80. DOI: 10.1016/j.cirpj.2022.06.009.

8. Bhanu, V., Gupta, A., and Pandey, C. 2022. Investigation on joining P91 steel and Incoloy 800HT through gas tungsten arc welding for Advanced Ultra Super Critical (AUSC) power plants. *Journal of Manufacturing Processes* 80: 558–80. DOI: /10.1016/J.JMAPRO.2022.06.029

9. Kim, W. G., Park, J. Y., Lee, H. Y., Hong, S. D., Kim, Y. W., and Kim, S. J. 2013. Time-dependent crack growth behavior for a SMAW weldment of Gr. 91 steel. *International Journal of Pressure Vessels and Piping* 110: 66–71. DOI: 10.1016/j.ijpvp.2013.04.024

10. Divya, M., Das, C. R. R., Albert, S. K. K., Goyal, S., Ganesh, P., and Kaul, R., et al. 2014. Influence of welding process on Type IV cracking behavior of P91 steel. *Materials Science and Engineering A* 613: 148–58. DOI: 10.1016/j.msea.2014.06.089

11. Ren, W., and Swindeman, R. 2010. A review of alloy 800H for applications in the Gen IV nuclear energy systems. *ASME Pressure Vessels and Piping Conference* 6: 821–36. DOI: 10.1115/PVP2010-25278

12. Albert, S. K., Kondo, M., Tabuchi, M., Yin, F., Sawada, K., and Abe, F. 2005. Improving the creep properties of 9Cr-3W-3Co-NbV steels and their weld joints by the addition of boron. *Metallurgical and Materials Transactions A* 36: 333–43. DOI: 10.1007/s11661-005-0306-x

13. Hariprasath, P., Sivaraj, P., Balasubramanian, V., Pilli, S., and Sridhar, K. 2022. Effect of the welding technique on mechanical properties and metallurgical characteristics of the naval grade high strength low alloy steel joints produced by SMAW and GMAW. *CIRP Journal of Manufacturing Science and Technology* 37: 584–95. DOI: 10.1016/J.CIRPJ.2022.03.007

14. Kumar, S. A., and Sathiya, P. 2015. Experimental investigation of the A-TIG welding process of incoloy 800H. *Materials and Manufacturing Processes* 30: 1154–9. DOI: 10.1080/10426914.2015.1019092

15. Baltušnikas, A., Lukošiūtė, I., Makarevičius, V., Kriūkienė, R., and Grybėnas, A. 2016. Influence of thermal exposure on structural changes of $M_{23}C_6$ carbide in P91 steel. *Journal of Materials Engineering and Performance* 25: 1945–51. DOI: 10.1007/s11665-016-2002-y

16. Ramkumar, K. D., Mulimani, S. S., Ankit, K., Kothari, A., and Ganguly, S. 2021. Effect of grain boundary precipitation on the mechanical integrity of EBW joints of Inconel 625. *Materials Science and Engineering A* 808: 140926. DOI: 10.1016/j.msea.2021.140926

17. Cieslak, M. J., Headley, T. J., and Romig, A. D. 1986. The welding metallurgy of HASTELLOY alloys C-4, C-22, and C-276. *Metallurgical Transactions A* 17: 2035–47. DOI: 10.1007/BF02645001

18. Pandey, C., Mahapatra, M. M., Kumar, P., and Saini, N. 2018. Dissimilar joining of CFEF steels using autogenous tungsten-inert gas welding and gas tungsten arc welding and their effect on δ-ferrite evolution and mechanical properties. *Journal of Manufacturing Processes* 31: 247–59. DOI: 10.1016/j.jmapro.2017.11.020

19. Francis, J. A., Mazur, W, and Bhadeshia, H. K. D. H. 2006. Type IV cracking in ferritic power plant steels. *Materials Science and Technology* 22: 1387–95.

20. Pandey, C., Mahapatra, M. M., Kumar, P., and Saini, N. 2017. Effect of normalization and tempering on microstructure and mechanical properties of V-groove and narrow-groove P91 pipe weldments. *Materials Science and Engineering A* 685: 39–49. DOI: 10.1016/J.MSEA.2016.12.079

21. Sakthivel, T., Syamala Rao, P., Parida, P. K. K., and Vasudevan, M. 2022. Transition of creep damage region in P91-Alloy800-SS316LN dissimilar metals weld joint. *Materials Letters* 306: 130915. DOI: 10.1016/j.matlet.2021.130915

22. Shah Hosseini, H., Shamanian, M., and Kermanpur, A. 2011. Characterization of microstructures and mechanical properties of Inconel 617/310 stainless steel dissimilar welds. *Materials Characterization* 62: 425–31. DOI: 10.1016/j.matchar.2011.02.003

23. Tan, L., Rakotojaona, L., Allen, T. R., Nanstad, R. K., and Busby, J. T. 2011. Microstructure optimization of austenitic Alloy 800H (Fe–21Cr–32Ni). *Materials Science and Engineering A* 528: 2755–61. DOI: 10.1016/j.msea.2010.12.052

24. Palanivel, R., Dinaharan, I., Laubscher, R. F., and Alarifi, I. M. 2021. Effect of Nd:YAG laser welding on microstructure and mechanical properties of Incoloy alloy 800. *Optics & Laser Technology* 140: 107039. DOI: 10.1016/j.optlastec.2021.107039

25. Rakoczy, Ł., Rutkowski, B., Grudzié N-Rakoczy, M., Cygan, R., Ratuszek, W., and Zielí Nska-Lipiec, A. 2020. Analysis of γ precipitates, carbides and nano-borides in heat-treated Ni-based superalloy using SEM, STEM-EDX, and HRSTEM. *Materials* 13(19): 4452. DOI: 10.3390/ma13194452

26. Zhou, W., Zhu, G., Wang, R., Yang, C., Tian, Y., and Zhang, L, et al. 2020. Inhibition of cracking by grain boundary modification in a non-weldable nickel-based superalloy processed by laser powder bed fusion. *Materials Science and Engineering A* 791: 139745. DOI: 10.1016/j.msea.2020.139745

27. Zhang, H., Gu, D., Ma, C., Guo, M., Yang, J., and Zhang, H, et al. 2021. Understanding tensile and creep properties of WC reinforced nickel-based composites fabricated by selective laser melting. *Materials Science and Engineering A* 802: 140431. DOI: 10.1016/j.msea.2020.140431

28. Kumar, A., and Pandey, C. 2022. Autogenous laser-welded dissimilar joint of ferritic/martensitic P92 steel and Inconel 617 alloy: mechanism, microstructure, and mechanical properties. *Archives of Civil and Mechanical Engineering* 22: 39. DOI: 10.1007/s43452-021-00365-6

29. Bhanu, V., Fydrych, D., Gupta, A., and Pandey, C. 2021. Study on microstructure and mechanical properties of laser welded dissimilar joint of P91 Steel and INCOLOY 800HT nickel alloy. *Materials* 14: 5876. DOI: 10.3390/ma14195876

30. ASTM E 23-12c. 2012. Standard test methods for notched bar impact testing of metallic materials. *Standards* 1–25. DOI: 10.1520/E0023-23A

31. Sims, C. T., Stoloff, N. S., and Hagel W. C. 1987. *Superalloys II*. New York: John Wiley & Sons.

VISHWA BHANU, **ANKUR GUPTA**, and **CHANDAN PANDEY** (*chandanpy.1989@gmail.com*) are with the Department of Mechanical Engineering, Indian Institute of Technology Jodhpur, Karwar, Jodhpur, India.